Co-intercalation-free Ether Electrolytes for Graphitic Anodes in Lithium-ion Batteries

Journal:	*Energy & Environmental Science*
Manuscript ID	EE-ART-05-2022-001489.R2
Article Type:	Paper
Date Submitted by the Author:	30-Sep-2022
Complete List of Authors:	Ma, Peiyuan; The University of Chicago Mirmira, Priyadarshini; University of Chicago, Pritzker School of Molecular Engineering Eng, Peter; The University of Chicago, Consortium for Advanced Radiation Sources Son, Seoung-Bum ; Argonne National Laboratory Bloom, Ira; Chemical Sciences and Engineering Division, Argonne National Laboratory Filatov, Alexander; The University of Chicago, Department of Chemistry Amanchukwu, Chibueze; The University of Chicago, Pritzker School of Molecular Engineering

Broader context

Energy dense batteries are required for the renewable energy transition. Lithium-ion batteries are state-of-the-art and have dominated the portable electronic market. However, for new applications such as electrified transport and the grid, additional requirements are needed such as higher energy density and wider working temperature range. Unfortunately, commercial carbonate electrolytes are unable to support batteries with these new requirements. While there has been innovation in anode and cathode design, electrolyte design has paled in comparison. For example, all Li-ion electrolytes use the same set of carbonate solvents, and utilize additives to effect some changes. Therefore, it is desired to develop novel electrolytes to replace carbonate electrolytes. Other classes of electrolytes such as ethers were studied historically but were abandoned because they suffer from ‘solvent co-intercalation,’ which leads to low specific energy and graphite exfoliation. Herein, we report a group of fluoroether solvents as the first class of ether solvent to inherently suppress solvent co-intercalation into graphite. Compared to carbonate electrolytes, these fluoroether electrolytes show better thermal stability and enable cycling of graphite-silicon composite anode with higher Coulombic efficiency. Our work indicates the impact of novel electrolyte development as an excellent route for improving Li-ion battery performance.

Co-intercalation-free Ether Electrolytes for Graphitic Anodes in Lithium-ion Batteries

Peiyuan Ma,[1] Priyadarshini Mirmira,[1] Peter J. Eng[3,4], Seoung-Bum Son[2], Ira D. Bloom[2],
Alexander S. Filatov[5] and Chibueze V. Amanchukwu[1*]

[1]Pritzker School of Molecular Engineering, University of Chicago, Chicago, IL 60637, USA

[2]Chemical Sciences and Engineering Division, Argonne National Laboratory, Lemont, IL 60439 USA

[3]Consortium for Advanced Radiation Sources, University of Chicago, Chicago, IL 60637, USA

[4]James Franck Institute, University of Chicago, Chicago, IL 60637, USA.

[5]Department of Chemistry, University of Chicago, Chicago, IL 60637, USA

*Corresponding author

Email: chibueze@uchicago.edu

Abstract

Carbonate-based electrolytes are widely used in Li-ion batteries but are limited by a small operating temperature window and poor cycling with silicon-containing graphitic anodes. The lack of non-carbonate electrolyte alternatives such as ether-based electrolytes is due to undesired solvent co-intercalation that occurs with graphitic anodes. Here, we show that fluoroethers are the first class of ether solvents to intrinsically support reversible lithium-ion intercalation into graphite without solvent co-intercalation at conventional salt concentrations. In full cells using graphite anode, they enable 10-fold higher energy densities compared to conventional ethers, and better thermal stability over carbonate electrolytes (operation up to 60°C) by producing a robust solvent-derived solid electrolyte interphase (SEI). As single-solvent-single-salt electrolytes, they remarkably outperform carbonate electrolytes with fluoroethylene carbonate (FEC) and vinylene carbonate (VC) additives when cycled with graphite-silicon composite anodes. Our molecular design strategy opens a new class of electrolytes that can enable next generation Li-ion batteries with higher energy density and wider working temperature window.

Introduction

Lithium-ion batteries are widely used to power portable electronics because of their high energy densities and have shown great promise in enabling the electrification of transport.[1] Fervent research to improve the performance of Li-ion batteries has led to novel anode materials beyond graphite such as silicon and cathode materials beyond $LiCoO_2$ such as $LiFePO_4$, $LiMn_2O_4$, and $LiNi_xMn_yCo_z$.[2–4] However, electrolyte innovation has paled in comparison, and all electrolytes used are still based on ethylene carbonate (EC), linear carbonates and $LiPF_6$. EC-based electrolytes are state-of-the-art because they enable reversible lithium (de)intercalation by surface passivation of graphite. However, the high melting point of EC and poor thermal stability of $LiPF_6$ salt limit the operating temperature window to −20°C to 40°C.[5] Moreover, carbonate electrolytes fail to support long term cycling of novel anode materials with higher specific capacities such as silicon or silicon-graphite composites.[6] Unlike graphite, the solid electrolyte interphase (SEI) between carbonate electrolytes and silicon is not robust enough to sustain the large volume change of silicon particles that happens during cycling, leading to continuous electrolyte degradation and rapid capacity decay.[7] Additives such as fluoroethylene carbonate (FEC) have been used to improve silicon compatibility of carbonate electrolytes but the continuous consumption of FEC and gas evolution still limit cycle life.[8] The lack of alternative Li-ion electrolytes has also stymied the growth of next generation cathode chemistries such as those based on low cobalt ($LiNiO_2$), high voltage ($LiCoPO_4$), and conversion cathodes such as sulfur and oxygen.[9–11]

Ether (glyme) compounds are promising candidates for the electrolyte solvent and have been explored for many different battery chemistries especially with lithium metal and silicon anodes because of their good reductive stability, low melting point and low viscosity.[5,12,13] However, when glymes are used in Li(or Na, K)-ion, batteries, ether molecules tend to insert into graphite together with alkali cation in a process termed 'solvent co-intercalation'. Solvent co-intercalation leads to instability of the graphite structure and significant decay in energy density: graphite electrodes cycled in glyme electrolytes can only achieve ~50% of theoretical graphite capacity with much higher operating potentials (> 1 V versus Li/Li^+ on average).[14–16] Hence, glymes have been deleterious for Li-ion batteries using graphitic anodes.

High concentration electrolytes (HCEs) and localized high concentration electrolytes (LHCEs) have been explored to suppress co-intercalation of ether solvents.[16–21] Their solvation structure is dominated by ion pairing, and solvent co-intercalation is suppressed by an anion-derived solid electrolyte interphase (SEI).[18] However, both HCEs and LHCEs must maintain a high salt/solvating solvent molar ratio (0.5~1) to suppress solvent co-intercalation because the co-intercalating tendency of ether solvent has not been changed.[22] Recent work by Dahn et al. has shown that lithium salt inventory loss within the electrolyte is a mode of battery degradation.[23] Hence, with HCEs and LHCEs, any loss in lithium inventory within the electrolyte during cycling may change the solvation structure and lead to undesired solvent co-intercalation.

Electrolyte chemistry provides a promising strategy for novel ether solvent development.[24] Several fluoroether solvents developed by us and others have been reported for lithium metal batteries, which covalently combine fluorine and ether building blocks.[25–28] In our previous work, we developed an "F1 family" of fluoroether electrolytes and studied their ion transport, thermal properties, electrochemical stability, ion solvation structure and stability with lithium metal.[27] In this work, we discover that these fluoroether solvents (Fig. 1a) can enable reversible lithium (de)intercalation within graphite. To the best of our knowledge, this is the first class of ether solvents that intrinsically prevents solvent co-intercalation at conventional salt concentrations (~1 M). Using X-ray diffraction (XRD), Raman spectroscopy and nuclear magnetic resonance (NMR), we show that fluoroether electrolytes enable desired graphite lithiation mechanism that forms Li_xC_6 phase without solvent co-intercalation. In graphite/LFP full cells, fluoroether electrolytes show cycling performance that mirrors commercial carbonate electrolyte at 20℃. Remarkably, fluoroether electrolytes enable superior cycling performance with graphite-silicon composite anodes that outperform carbonate electrolyte containing fluoroethylene carbonate (FEC) and vinylene carbonate (VC) additives. Fluoroethers also have superior thermal stability compared to commercial carbonate electrolytes and they show better cycling performance at 60℃ in graphite or graphite-silicon based cells. Investigations on the solid electrolyte interphase (SEI) reveal that fluoroether compounds decompose and contribute to the formation of LiF-rich SEI, which likely suppresses solvent co-intercalation. Our study opens a new direction for developing novel carbonate-free electrolytes for Li-ion batteries that can expand the operational temperature range and allow for the incorporation of novel electrode chemistries.

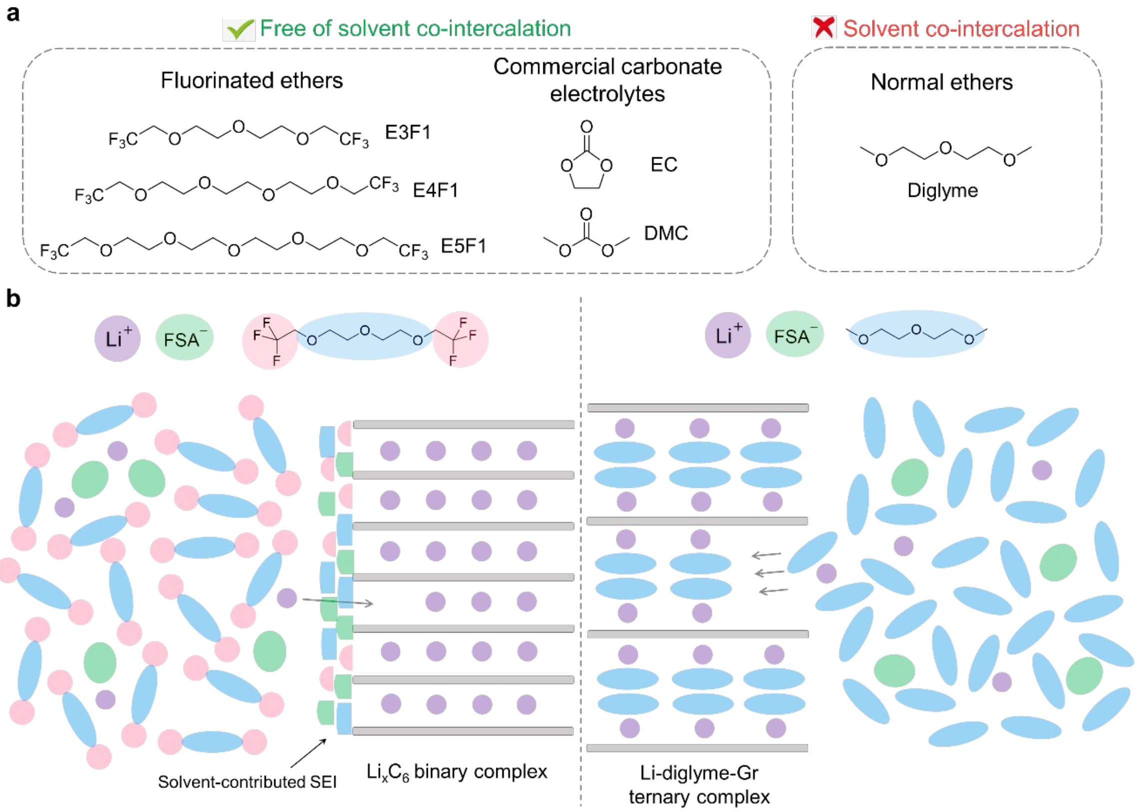

Fig. 1 | Project overview. a) Molecular structure of solvents studied in this work. **b)** Illustration of the influence of fluorination on ether solvent performance with graphite electrode: Fluorinated ethers (E3F1) can suppress solvent co-intercalation by passivating graphite surface with a solvent-derived solid electrolyte interphase (SEI) while normal ethers (e.g., diglyme) tends to co-intercalate due to the lack of a robust SEI.

Enabling reversible lithium-ion (de)intercalation with fluoroethers

The influence of electrolyte selection on lithium intercalation behavior was first studied in lithium metal/graphite (Li/Gr) half cells. Li/Gr cells using 1 M lithium bis (fluorosulfonyl) amide (LiFSA) in E3F1, 1 M $LiPF_6$ in ethylene carbonate/dimethyl carbonate (EC/DMC), and 1 M LiFSA in diglyme as electrolytes were first explored using cyclic voltammetry (CV). Fig. 2a shows that the E3F1 cell and EC/DMC cell have similar reduction peaks from 0.5 V to 0.01 V, which corresponds to graphite lithiation reactions. In the following reverse scan, delithiation peaks are observed in E3F1 and EC/DMC cells around 0.25 V. However, the CV curve of diglyme electrolyte shows multiple weak and broad peaks between 2 V and 0.01 V, characteristic of the solvent co-intercalation reaction.[14] Fig. 2b shows the first galvanostatic cycle of Li/Gr cells using the same set of electrolytes at a current rate of C/20 (1 C ≈ 2.17 mA cm^{-2}). Similar to the CV, the voltage profile of the E3F1 cell mimics the EC/DMC cell by having a stable voltage plateau below 0.2 V and achieving a first cycle deintercalation capacity of 354.2 mAh g^{-1} in a Coulombic efficiency of 87.6%. In contrast, Li/Gr cell with 1 M LiFSA in diglyme as the electrolyte exhibits higher intercalation potential (~1 V), low deintercalation capacity (101.2 mAh g^{-1}) and low Coulombic efficiency (53.2%). The poor behavior of graphite cycling observed in 'normal ethers' such as diglyme has been attributed to solvent co-intercalation.[14] Fig. 2c shows that 0.5 M LiFSA in E3F1 electrolyte and other synthesized fluoroethers (E4F1 and E5F1) also enable reversible lithium (de)intercalation voltage profile with graphite, mimicking 1 M LiFSA in E3F1. Hence, electrochemical characterizations indicate that these fluoroether electrolytes are intrinsically able to support reversible lithium (de)intercalation and do not depend on high salt concentration or diluents in the manner observed for HCEs and LHCEs.[16–22] Long term cycling of Li/Gr cells was also performed. As Fig. S1 shows, E3F1, E4F1 and EC/DMC electrolytes can support stable Li/Gr cell cycling for 60 cycles at a current rate of C/10 while the Li/Gr cell using diglyme electrolyte shows lower capacity and very rapid capacity decay. However, it is difficult to decouple the effects of lithium metal cycling efficiency and electrolyte degradation when comparing fluoroether electrolytes and EC/DMC electrolyte in Li/Gr long term cycling.

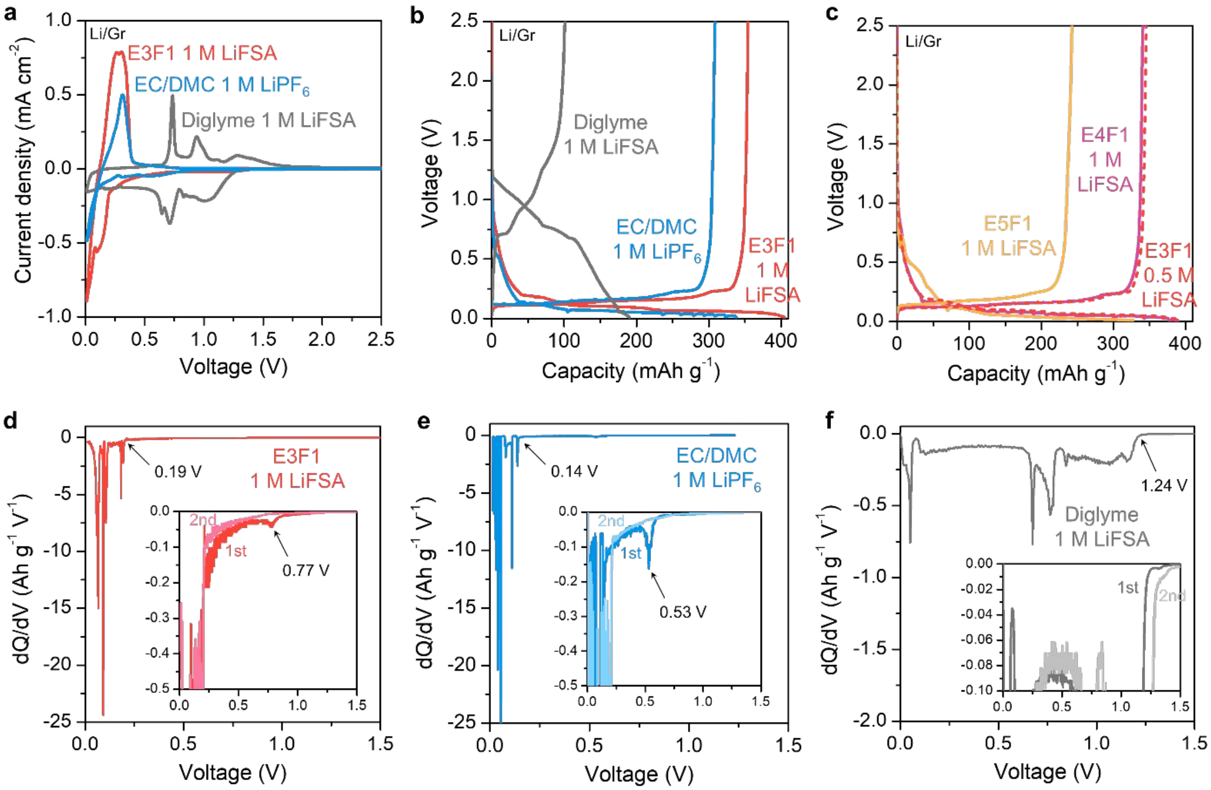

Fig. 2 | Electrochemical performance in half cells. **a**, Cyclic voltammetry of lithium/graphite (Li/Gr) cells using 1 M LiFSA in E3F1, 1 M LiFSA in diglyme and 1 M LiPF$_6$ in EC/DMC as electrolytes at a scan rate of 0.05 mV s^{-1} from open circuit voltage to 0.01 V and then reverse scanned to 2.5 V. **b-c**, The first galvanostatic cycle of Li/Gr half cells at a current rate of C/20 (1 C ≈ 2.17 mA cm^{-2}): **b**, Voltage profiles of Li/Gr cells using 1 M LiFSA in E3F1, 1 M LiFSA in diglyme and 1 M LiPF$_6$ in EC/DMC. **c**, Voltage profiles of Li/Gr cells using 1 M LiFSA in E4F1, 1 M LiFSA in E5F1 and 0.5 M LiFSA in E3F1. **d-f**, First-order derivatives of the first cycle graphite intercalation voltage profiles in Li/Gr cells using (**d**) 1 M LiFSA in E3F1, (**e**) 1 M LiPF$_6$ in EC/DMC and (**f**) 1 M LiFSA in diglyme. The insets in **d-f** are enlarged views with the differential curves of both the first and second intercalation for comparison.

To investigate the details of lithium (solvent) insertion, differential analysis was performed on the Li/Gr cell voltage profiles discussed above. First-order derivatives of capacity-voltage curves (dQ/dV) were calculated numerically and plotted as a function of cell voltage. Fig. 2d shows the dQ/dV curve for the first lithiation using E3F1 electrolyte. Several sharp peaks arise below 0.19

V, which resemble the different stages of graphite lithiation reaction without solvent co-intercalation like in EC/DMC electrolytes.[29] On the contrary, Fig. 2f shows that diglyme electrolyte leads to broad peaks starting from 1.24 V, corresponding to the high potentials of solvent co-intercalated lithiation.[14] The tiny peak around 0.77 V shown in the inset of Fig. 2d suggests the formation of solid electrolyte interphase (SEI) in E3F1 electrolyte. Fig. 2e shows that EC/DMC electrolyte also has a SEI formation peak at 0.53 V. However, no such SEI formation peak is observed for diglyme. Differential analysis reinforces the mechanistic similarity between EC/DMC and E3F1 and the contrast between E3F1 and diglyme in graphite intercalation behavior.

Ex-situ characterization of graphite intercalation compounds

The lithium intercalation mechanism in fluoroether electrolytes was studied using a suite of diffraction and spectroscopic techniques. Intercalated graphite electrodes were retrieved from Li/Gr cells after intercalating to 0.01 V or 20 hours at a current rate of C/20. Fig. S2 shows the digital photos of intercalated graphite, where the E3F1, E4F1 sample has a golden color like the EC/DMC sample while the diglyme sample retains a black color. This suggests that fluoroethers produce graphite intercalation compounds (GICs) like EC/DMC but different from diglyme. Fig. 3a shows *ex situ* X-ray diffraction (XRD) patterns of graphite intercalated in different electrolytes with pristine graphite for comparison. Pristine graphite has a (002) peak at $2\theta = 26.5°$ and a (004) peak at $2\theta = 54.6°$, corresponding to a graphite interlayer distance of 3.36 Å. After lithium-ion insertion in E3F1, E4F1 and EC/DMC electrolytes, graphite (002) and (004) peaks shift to lower diffraction angles due to lattice expansion. The splitting of graphite peaks in these lithiated samples indicates the coexistence of two stages.[30] The (002) peak at $2\theta = 24.0°$ and (004) peak at $2\theta = 49.1°$ are assigned to stage-1 LiC_6 phase with a graphite interlayer distance of 3.70 Å. Stage-2 $Li_{0.5}C_6$ phase produces a (002) peak at $2\theta = 25.3°$ and a (004) peak at $2\theta = 51.9°$ with a graphite interlayer distance of 3.52 Å. The calculated interlayer distance values agree with literature reports.[31,32] The formation of Li_xC_6 GICs in fluorinated ether electrolytes agrees with the electrochemical observations discussed earlier and proves the ability of these electrolytes to suppress solvent co-intercalation. On the contrary, the graphite electrode intercalated in the diglyme electrolyte shows a series of peaks at $2\theta = 15.8°, 23.8°, 31.9°$ and

40.2° as marked by triangle symbols. These peaks correspond to the (002), (003), (004) and (005) peaks of solvent co-intercalated ternary GICs as reported by many others. (The unit cell of ternary GICs has been changed to containing only one graphene layer following literature convention).[14,15]

To complement the diffraction data, Raman spectroscopy was also used to characterize intercalated graphite electrodes. Fig. S3 shows that Raman spectra were collected from 'shiny' graphite particles to ensure reproducibility across samples. Fig. 3b shows that pristine graphite has a so-called graphitic "G band" around 1580 cm^{-1} and a disordered "D band" around 1330 cm^{-1}. When graphite is lithiated in EC/DMC, E3F1 and E4F1 electrolytes, both G and D bands diminished, which indicates they produce Li_xC_6 insertion complexes.[33] In contrast, the Raman spectra of graphite intercalated in diglyme electrolyte shows a split G band, which is characteristic of 'partially lithiated' graphite.[33]

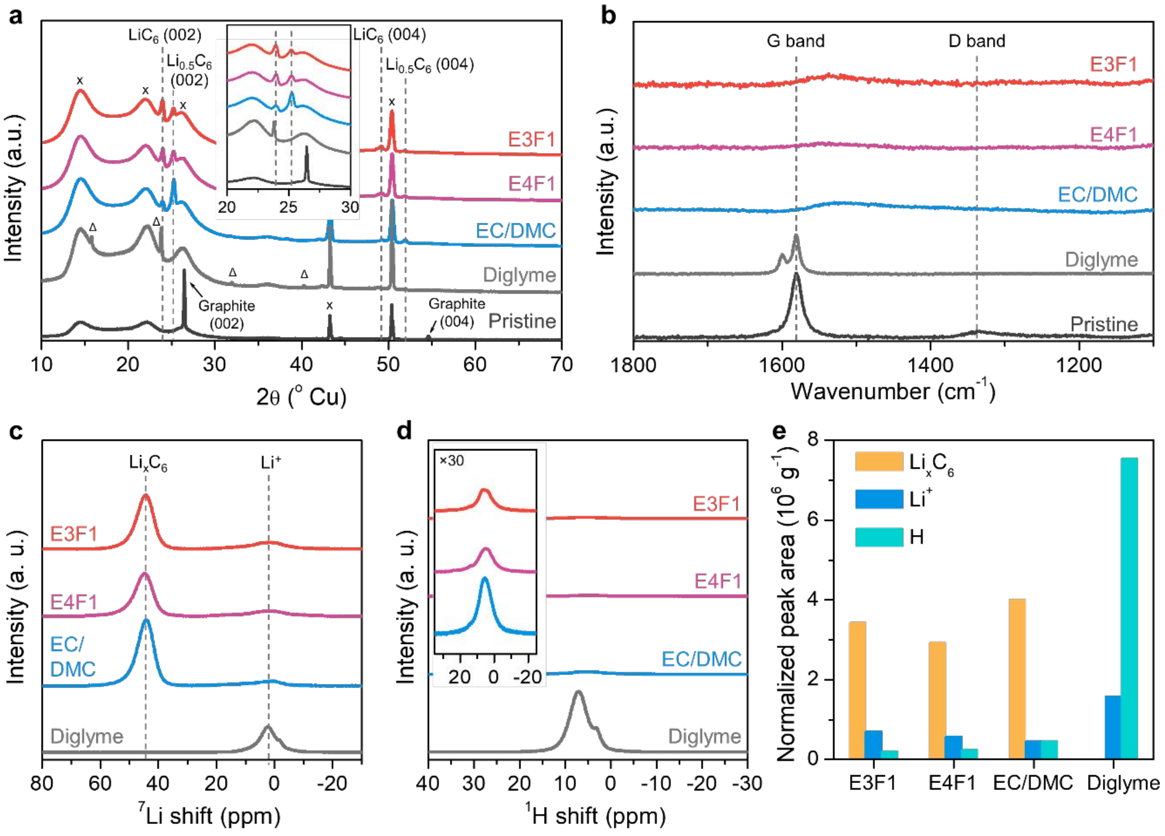

Fig. 3 | Ex-situ characterization of intercalated graphite. Characterizations of graphite electrodes intercalated in 1 M LiFSA in E3F1 (E3F1), 1 M LiFSA in E4F1 (E4F1), 1 M $LiPF_6$ in EC/DMC (EC/DMC) and 1 M LiFSA in diglyme (diglyme) electrolytes. **a**, XRD patterns of intercalated graphite with pristine graphite as control. x: background peaks from copper and polyimide substrates; Δ: (002), (003), (004) and (005) peaks of ternary GIC (from left to right). The inset shows an enlarged view of the region from $2\theta = 20^o$ to 30^o. **b**, Raman spectra of intercalated graphite with pristine graphite as control. **c-e**, Solid state MAS NMR of intercalated graphite: **c**, ^7Li NMR spectra; **d**, ^1H NMR spectra (the inset shows spectra magnified 30 times); **e**, Normalized peak integrations. NMR spectra intensity and peak integrations were normalized by number of scan and sample mass.

Solid state magic angle spinning (MAS) NMR spectroscopy was used to further investigate the composition of intercalated graphite electrodes. Fig. 3c shows ^7Li NMR spectra of graphite intercalated in E3F1, E4F1, EC/DMC and diglyme electrolytes. The strong peak around 45 ppm is assigned to Li_xC_6 GICs in E3F1, E4F1 and EC/DMC samples, according to prior work.[34] A relatively weak peak around 2 ppm is also observed for Li^+ species in the SEI and potentially any salt residue. For the diglyme sample, no Li_xC_6 peak is observed and the intensity of the Li^+ peak (2 ppm) appears stronger, likely due to the presence of solvent co-intercalated ternary GIC. Fig. 3d and 3e show that the diglyme sample also has an order of magnitude higher abundance of protons than other samples, which corresponds to the co-intercalated diglyme molecules. E3F1 and E4F1 samples have much lower residual proton signals, which is at the same order of magnitude as EC/DMC. Hence, solid state NMR further confirms the formation of Li_xC_6 and the absence of solvent co-intercalation in fluoroether electrolytes.

Intercalation mechanism revealed by *in situ* synchrotron XRD

To explore the mechanism of lithium insertion and exclude the effects of sample preparation, *in situ* synchrotron X-ray diffraction (XRD) was performed on lithium/graphite (Li/Gr) cells. Fig. S4 shows the configuration of Li/Gr coin cells for *in situ* XRD experiments with Kapton windows. Fig. S5 shows that the voltage profiles of *in situ* and normal coin cells are similar, which indicates that electrochemistry is barely affected by beamline exposure. Fig. 4a shows *in situ* XRD patterns aligned with voltage profile for the Li/Gr cell using 1 M LiFSA in E3F1 as electrolyte. Before lithiation, the (002) peak of pristine graphite is observed at $2\theta = 26.5°$, corresponding to an interlayer distance of 3.36 Å. At the beginning of lithiation, the graphite interlayer diffraction peak (002) gradually shifts to lower diffraction angles due to the expansion of lattice, but no clear stage distinction is observed. When the voltage drops below 0.04 V, the graphite interlayer diffraction peak settles at $2\theta = 25.3°$, corresponding to the (002) peak of the stage-2 phase with an interlayer distance of 3.52 Å. Simultaneously, a new peak emerges at $2\theta = 24.0°$, originating from the stage-1 phase with an interlayer distance of 3.70 Å. Thereafter, further lithium insertion leads to phase transition from stage-2 to stage-1 phase. Graphite interlayer distance was calculated according to Bragg's law and summarized in Fig. 4c. Excellent reversibility of lithium intercalation with E3F1 electrolyte is illustrated by the symmetrical evolution of XRD patterns during delithiation. Fig. S6 shows that the *in situ* XRD results of the E4F1 cell mimic the E3F1 cell as expected. Reynier et al. and He et al. reported *in situ* XRD studies of graphite cycled in carbonate electrolytes.[31,32] They observed shifting and splitting of the graphite (002) peak in a similar manner, which indicates fluoroether electrolytes share the same lithium insertion mechanism with commercial carbonate electrolytes.

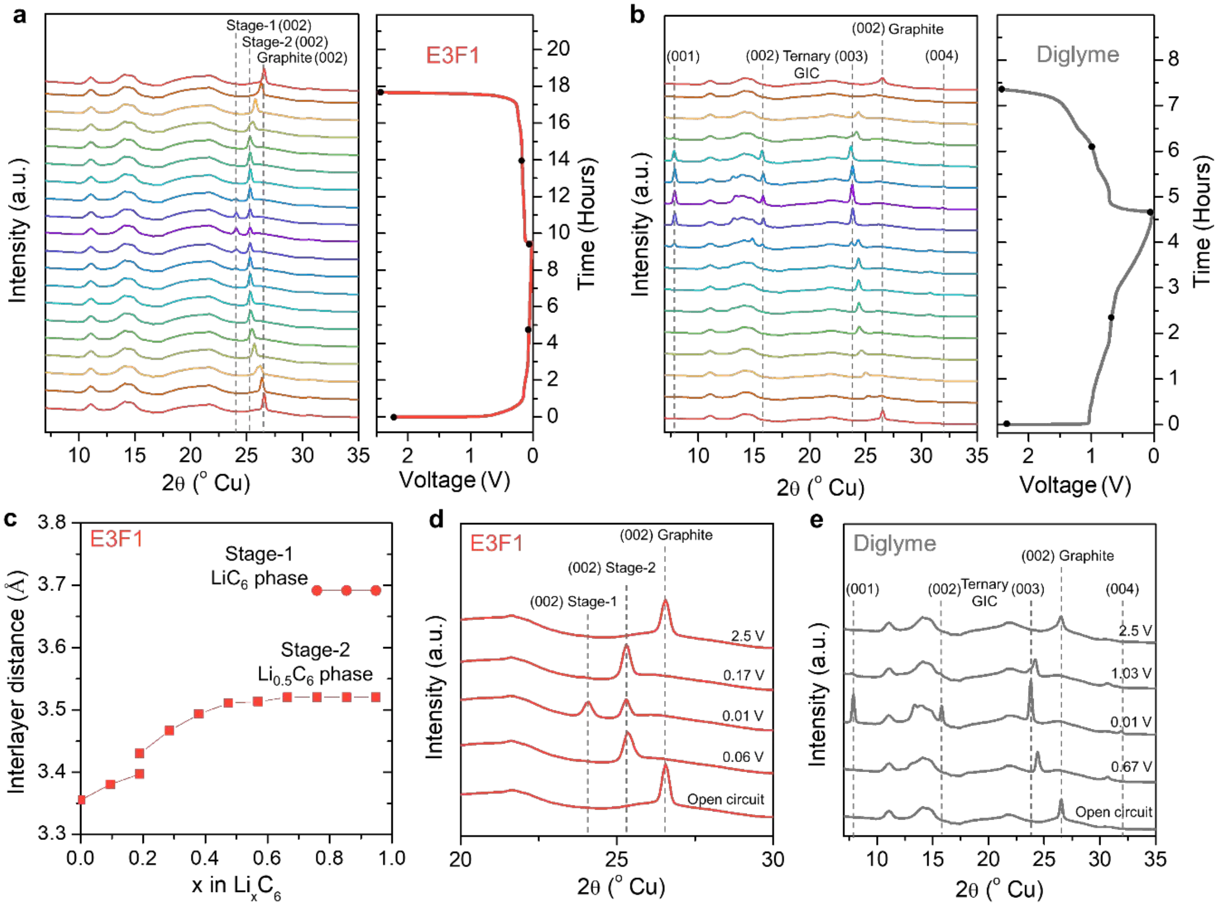

Fig. 4 | *in situ* synchrotron X-ray diffraction (XRD). a-b, Time-aligned XRD patterns and voltage profiles of Li/Gr cells using (**a**) 1 M LiFSA in E3F1 and (**b**) 1 M LiFSA in diglyme as electrolytes. **c**, The evolution of graphene interlayer distance when graphite is lithiated in E3F1 electrolyte. **d-e**, Enlarged view of XRD patterns at selected points of cycling (marked by black dots in **a** and **b**). The cells were cycled at a current rate of C/10 while XRD patterns were collected.

In contrast, diglyme electrolyte leads to drastically different XRD patterns as shown in Fig. 4b. In addition to the shifting of the original graphite (002) peak, a series of new peaks at 2θ = 7.9°, 13.4°, 15.8°, 23.8° and 31.9° arise at the later stage of intercalation. Kim et al. reported that those peaks originate from the co-intercalated glyme solvent layers.[15] The peaks at 2θ = 7.9°, 15.8°, 23.8° and 31.9° are assigned as (001), (002), (003) and (004) peaks of Li-diglyme-graphite ternary GIC with a graphite interlayer distance of 11.18 Å, in agreement with literature.[14,15] The peak at 2θ = 13.4° probably originates from in-plane superstructural ordering of intercalated ion and solvent complexes.[35]

Fig. 4d and 4e summarized XRD patterns at several key points as marked by black dots in the voltage profiles. The (002) peak of graphite is well recovered in the E3F1 cell after delithiation, indicating good reversibility of graphite structure change. However, the (002) peak of graphite broadens significantly after just one cycle in the diglyme electrolyte, which suggests solvent co-intercalation likely perturbs the layered graphite structure. The poor reversibility of graphite structure in diglyme explains its rapid capacity decay in full cell cycling (Fig. 5a). Such distinction is supported by *ex situ* Raman spectroscopy and XRD of deintercalated graphite sample as shown in Fig. S7 and S8. Despite different charging rates and sample preparation processes, *ex situ* testing results corroborate the *in situ* XRD results. They provide mutual confirmation for the graphite intercalation mechanism and prove the absence of solvent co-intercalation in fluoroether electrolytes.

Long term cycling in full cells

The benefits of eliminating solvent co-intercalation were verified by graphite/$LiFePO_4$ (Gr/LFP) full cell cycling. Gr/LFP cells were cycled at a current rate of C/3 after three formation cycles at C/20 (1 C $\approx$ 1.81 mA cm^{-2}, N/P $\approx$ 1.2). Fig. 5a and S9 show that E3F1 electrolyte enables similar voltage profiles and capacity retention with EC/DMC electrolyte in Gr/LFP long term cycling. By contrast, diglyme electrolyte leads to much lower discharge capacities due to solvent co-intercalation. The E3F1 cell can retain 92 mAh g^{-1} capacity at the 100th cycle, which is 6 times higher than the diglyme cell. As Fig. S9 shows, solvent co-intercalation mechanism also leads to the lower cell voltage of the diglyme cell. Therefore, E3F1 cells have energy density 10 times higher than diglyme cells (calculated from discharge capacity at the 100th cycle).

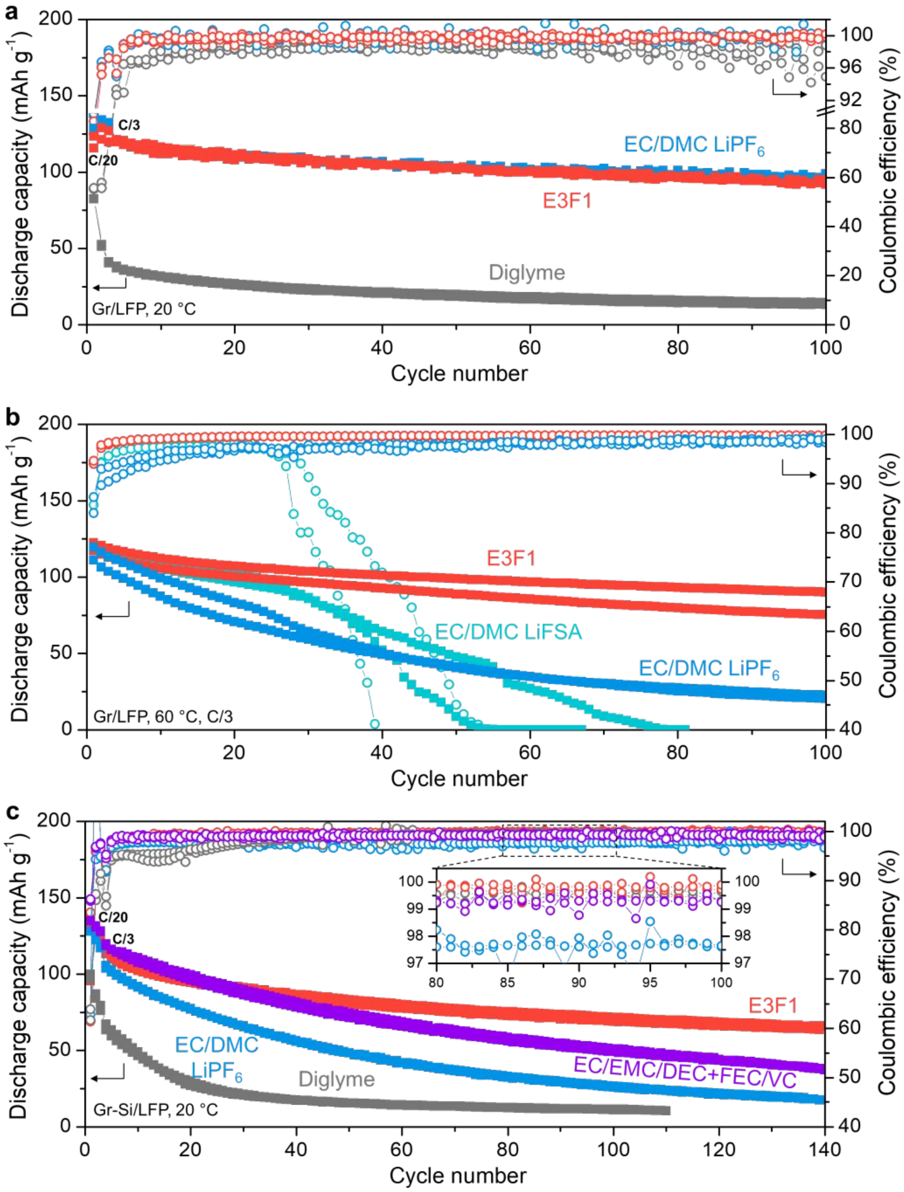

Fig. 5 | Cycling performance in full cells. a, Galvanostatic cycling of graphite/$LiFePO_4$ (Gr/LFP) full cells at 20°C using 1 M LiFSA in E3F1 (E3F1), 1 M LiFSA in diglyme (diglyme) and 1 M $LiPF_6$ in EC/DMC (EC/DMC $LiPF_6$). **b**, Galvanostatic cycling of Gr/LFP full cells at 60°C using E3F1 electrolyte, EC/DMC $LiPF_6$ electrolyte and 1 M LiFSA in EC/DMC (EC/DMC LiFSA). Three formation cycles at C/20 were performed at 20°C prior to 60°C cycling. **c**, Galvanostatic cycling of graphite-silicon composite/$LiFePO_4$ (Gr-Si/LFP) full cells at 20°C using E3F1 electrolyte, diglyme electrolyte, EC/DMC $LiPF_6$ electrolyte and 1.2 M $LiPF_6$ in EC/EMC/DEC+2% FEC+1%VC (EC/EMC/DEC+FEC/VC). Two replicate cells of each test are shown. EMC (ethyl methyl carbonate); DEC (diethyl carbonate); FEC (fluoroethylene carbonate); VC (vinylene carbonate).

Fluoroether electrolytes have superior thermal stability over carbonate electrolytes as manifested by cell cycling at 60°C. Fig.5b shows that Gr/LFP full cells using E3F1 electrolyte can be cycled repeatedly at 60°C and their capacity retention is comparable to cycling at 20°C (~69% vs. ~77% at 100th cycle, all values in this section are averaged from two replicates). However, Gr/LFP cells using EC/DMC $LiPF_6$ electrolyte show rapid capacity decay and lower Coulombic efficiencies at the onset. At the 100th cycle, EC/DMC $LiPF_6$ electrolyte can only maintain ~19% of the original discharge capacity, which is much lower than its 20°C cycling performance (~79%). Despite better capacity retention in the initial 30 cycles, the capacity of Gr/LFP cell using EC/DMC LiFSA electrolyte decays rapidly afterward. As shown in Fig. S10, the E3F1 cell has stable overpotential throughout 100 cycles, evidencing good stability at 60°C. The overpotential of EC/DMC $LiPF_6$ cell keeps growing with cycle number, indicating continuous electrolyte degradation.[36–38] Both Fig. 5b and S10 show that EC/DMC LiFSA cells struggle because of poor reversibility at later cycles. Fig. S11 shows the cycling of Li/Gr half cells at 60°C which helps to explain the different decaying modes of full cells. EC/DMC $LiPF_6$ electrolyte shows Coulombic efficiency lower than the E3F1 electrolyte, which corresponds to continuous degradation of EC/DMC $LiPF_6$ at 60°C. The Coulombic efficiency of EC/DMC LiFSA is higher than EC/DMC $LiPF_6$ and close to E3F1. However, the discharge capacity of EC/DMC LiFSA cell decays faster, which suggests the depletion of anode capacity might cause the rapid decay of EC/DMC LiFSA full cells at later cycles. The cycling performance at 60°C and 20°C shows that E3F1 electrolyte can afford a broader working temperature window and is an exemplary electrolyte candidate for Li-ion batteries.

To show the distinctive advantage of fluoroether electrolytes over carbonate electrolytes in enabling novel Li-ion batteries, graphite-silicon (Gr-Si) based half cell and full cell cycling was performed. As shown in Fig. 5c, E3F1 electrolyte clearly outperforms EC/DMC $LiPF_6$ and diglyme electrolyte in Gr-Si/LFP full cells ($1\ C \approx 1.81\ mA\ cm^{-2}$, $N/P \approx 1.3$) with higher discharge capacity and Coulombic efficiency throughout cycling. Fig. S12 and S13 show that diglyme still co-intercalates into Gr-Si, which likely leads to the fast capacity decay of diglyme full cells from the beginning. Although the EC/EMC (ethyl methyl carbonate)/DEC (diethyl carbonate) electrolyte with FEC (fluoroethylene carbonate) and VC (vinylene carbonate) additives shows improved cycling stability compared to EC/DMC, the inset of Fig. 5c shows that its Coulombic efficiency is still lower than E3F1. As a result, E3F1 electrolyte retains discharge capacity higher than EC/EMC/DEC+FEC/VC at the 140th cycle (65 mAh g^{-1} vs. 38 mAh g^{-1}). Fig. S14 shows that E3F1 electrolyte also has higher Coulombic efficiency over carbonate electrolytes in Li/Gr-Si half cell cycling. To show that the thermal stability of E3F1 is independent of battery chemistry, Fig. S15 and S16 show that the Li/Gr-Si half cells and Gr-Si/LFP full cells using E3F1 electrolyte maintain their better cycling performance over carbonate electrolytes at 60°C. The superior cycling performance of E3F1 electrolyte with Gr-Si anode proves its advantage in enabling novel silicon-based Li-ion batteries with higher energy density.

Graphite/electrolyte interface passivated by fluoroether solvents

It is widely accepted that the solid electrolyte interphase (SEI) composition and structure plays a vital role in enabling reversible lithium (de)intercalation and long-term Li-ion battery cycling.[5,39,40] The formation of SEI in fluoroether electrolytes was first indicated by dQ/dV analysis of Li/Gr cell voltage profiles as discussed above. Electrochemical impedance spectroscopy (EIS) studies on Gr/LFP cells shown in Fig. S17 and Table S1 also indicate a more resistive interfacial layer in E3F1 as compared to diglyme. Transmission electron microscopy (TEM) and energy-dispersive X-ray spectroscopy (EDS) were also used to verify the formation of SEI in E3F1 1 M LiFSA electrolyte. Fig. S18a-b show that E3F1 electrolyte produces a homogeneous SEI with thickness around 50 nm at the interface with graphite. Fig. S18c-g show the corresponding EDS mapping, where fluorine and oxygen elements are observed to concentrate in the inner layer (close to graphite surface) of the SEI while the outer layer of SEI contains more carbon and sulfur elements. As discussed later, the SEI elemental composition determined by EDS is verified by other characterization techniques.

X-ray photoelectron spectroscopy (XPS) was used to characterize the chemical composition of graphite SEI. To exclude the interference of PVDF binder, a graphite electrode using styrene-butadiene rubber (SBR) binder was prepared and used for XPS characterization (see experimental section). Three electrolytes: 1 M LiFSA in E3F1, 1 M LiFSA in diglyme and E3F1 saturated with $LiClO_4$ (< 0.1 M) were studied to decipher the role of solvent and salt in interfacial passivation. Fig. S19 shows the voltage profile of corresponding Li/Gr cell cycling, where E3F1 $LiClO_4$ electrolyte can still avoid solvent co-intercalation despite its very low salt concentration. Fig. 6a shows the C1s XPS spectra, where all three samples have similar C−O (286.0 eV) and C−C (284.6 eV) components while the E3F1 $LiClO_4$ sample has more carbonate (290.2 eV) component. In addition, a signal for Li_xC_6 (283.6 eV) component is present only for E3F1 $LiClO_4$, which might be caused by uneven delithiation due to the limited electrolyte conductivity. Fig. 6b shows that all three samples have similar O1s XPS spectra. Fig. 6c shows the F1s XPS spectra, where E3F1 LiFSA leads to more LiF compared to diglyme LiFSA. In addition, C−F (688.4 eV) components are observed for E3F1 samples with low intensity. As discussed later, the presence of C−F components in SEI is also supported by solution state NMR and likely corresponds to the organic degradation products of E3F1. When LiFSA salt is replaced by $LiClO_4$, E3F1 $LiClO_4$ electrolyte still produces LiF in the SEI with lower concentration. This indicates E3F1 solvent molecules do degrade at the graphite interface and contribute to a LiF-rich SEI. Given the similarity between E3F1 LiFSA and diglyme LiFSA samples in C1s and O1s XPS spectra, the additional LiF and organic components produced by E3F1 reductive degradation likely play a role in preventing solvent co-intercalation.

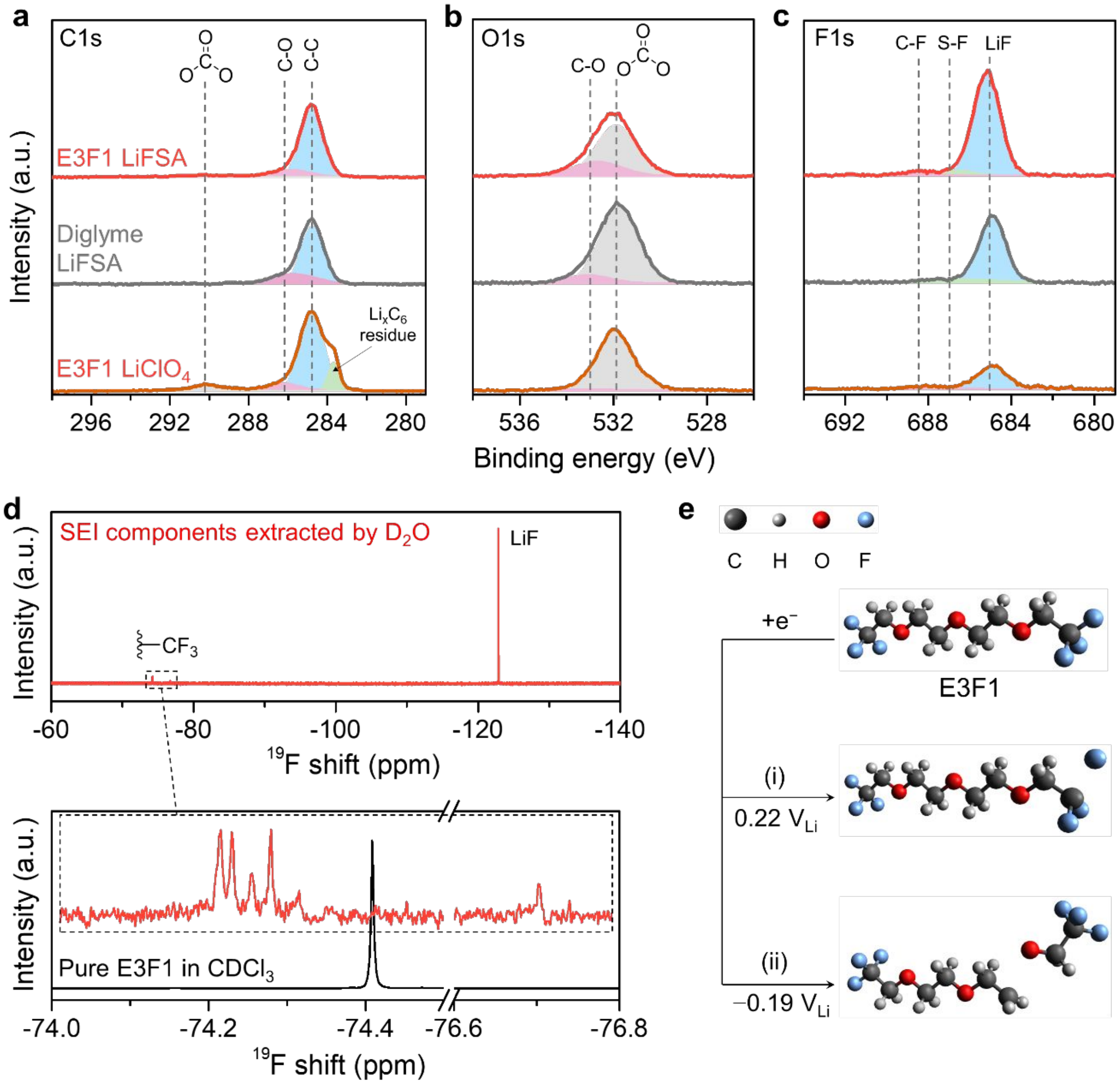

Fig. 6 | Interfacial properties. a-c, XPS of graphite electrodes retrieved from corresponding Gr/Li cells after formation cycles (ending on deintercalation): **a**, C1s spectra; **b**, O1s spectra; **c**, F1s spectra. **d**, ^{19}F NMR spectra of E3F1 1 M LiFSA derived SEI components dissolved in D_2O. Inset shows an enlarged view of the CF_3 peaks and the ^{19}F NMR of pure E3F1 in $CDCl_3$ for comparison. **e**, Reductive degradation pathways and corresponding adiabatic reduction potentials of E3F1 predicted by DFT calculations (V_{Li}: volts versus Li/Li$^+$).

NMR spectroscopy was also used to probe SEI composition and the degradation of E3F1 solvent. Graphite sample cycled in E3F1 1 M LiFSA electrolyte was extracted by D_2O and the extract was analyzed by solution state NMR (see experimental section for preparation procedure). Fig. 6d shows the proton-decoupled ^{19}F NMR spectra of SEI components extracted by D_2O, where a single peak for LiF (−123 ppm) and multiple peaks for $-CF_3$ groups (−74 ppm) are detected. Compared to the NMR spectra of pure E3F1 solvent, the organic species in D_2O extract have similar functional groups but are apparently not just pristine E3F1. As shown in Fig. 6e and Fig. S20, density functional theory (DFT) calculations have predicted that the reductive degradation of E3F1 is favored above 0 V versus Li/Li$^+$, which generates LiF and organic fragments maintaining similar structure with E3F1. While LiF is detected by ^{19}F NMR, the other signals around –74 ppm very likely correspond to E3F1-derived organic components in the SEI. Fig. S21 shows that ^{1}H NMR spectra of D_2O extracted SEI components also have multiple peaks for ether-like protons. However, it is currently difficult to separate and determine the exact structure of those degradation products. Combining the evidence from TEM, EDS, XPS and NMR, it is clear that E3F1 solvent participates in the passivation of graphite interface.

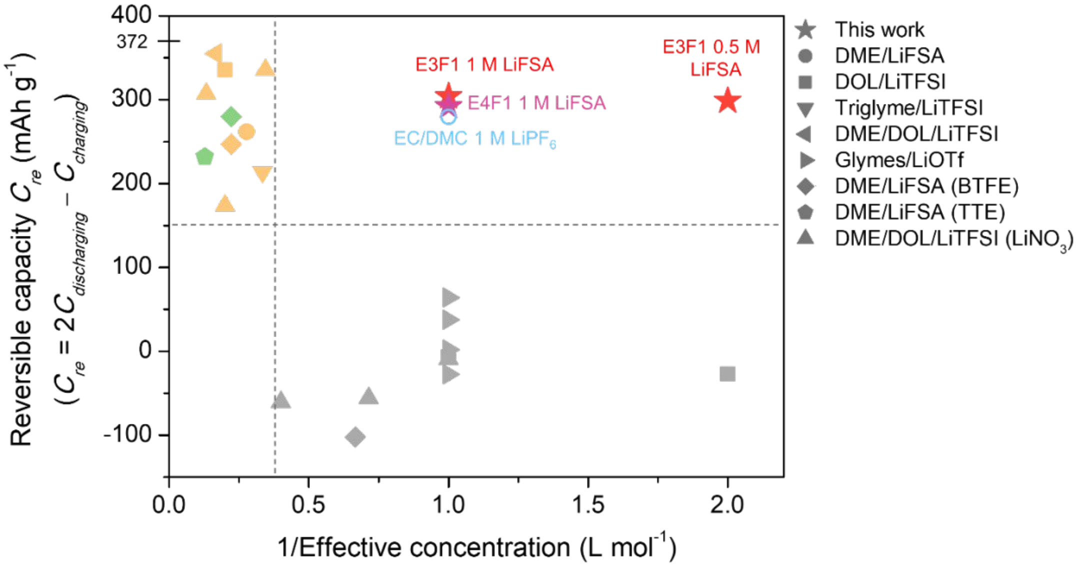

Fig. 7 | Comparison of ether electrolytes for lithium-ion batteries. Fluoroethers studied in this work are the only group of ether solvents that can achieve high performance with graphite anodes at conventional salt concentrations. Most normal ether electrolytes with conventional salt concentrations show poor performance with graphite (grey color symbols). High (effective) salt concentrations are required for ether-based HCEs (yellow color symbols) and LHCEs (green color symbols) to enable high reversible capacity. Reversible capacity, defined as 2×deintercalation capacity – intercalation capacity, was extracted from data of Li/Gr cells in corresponding references: DME/LiFSA,[19] DOL/LiTFSI,[41] triglyme/LiTFSI,[16] DME/DOL/LiTFSI,[20] Glymes/LiOTf,[14] DME/LiFSA(BTFE),[22] DME/LiFSA(TTE)[42] and DME/DOL/LiTFSI($LiNO_3$).[43] To account for realistic solvation structures, effective concentration is defined as molar concentration of salt in the volume of solvating solvent, where non-solvating diluents such as BTFE and TTE are excluded.

Outstanding performance among ethers reported in literature

To be best of our knowledge, the fluoroethers reported in this work are the first class of ether solvents that can inherently suppress solvent co-intercalation into graphite. Fig. 7 compares this work to other ether electrolytes whose performance with graphite electrode has been studied in literature. Reversible capacity is defined as 2 × (1st deintercalation capacity) – (1st intercalation capacity) and should be 372 mAh g^{-1} for ideal electrolytes.[43] We define “effective concentration” as salt concentration in solvating solvents (excluding diluents). Hence, effective concentration equals to reported salt concentration for most cases. But for LHCEs, effective concentration is estimated from (mol of salt)/(volume of solvating solvent). Most ether solvents co-intercalate into graphite at conventional concentrations (< 3 M), which leads to reversible capacity below 150 mAh g^{-1}. As shown in Fig. S22, the addition of SEI-formation additives such as FEC fails to suppress solvent co-intercalation in diglyme electrolytes. To suppress solvent co-intercalation, high salt concentrations are typically used (HCEs). For LHCEs, although the superficial concentration is close to 1.5 M, the effective concentration is still as high as HCEs since the diluents cannot dissolve any salt. Only the fluoroethers presented in this work achieve high reversible capacity (~300 mAh g^{-1}) at effective concentration close to 1 M, similar to commercial carbonates. Additionally, these fluoroethers passivate graphite electrode with a solvent-derived SEI while HCEs and LHCEs have been reported to produce an anion-derived SEI.[37,42] Therefore, fluoroethers in this work can inherently suppress solvent co-intercalation without the need for high salt concentration. Preliminary studies on other fluoroethers such as fluorinated 1,4-dimethoxylbutane (FDMB, Fig. S23) show that the ability to suppress solvent co-intercalation is not limited to the fluoroethers studied here.

Conclusions

In this work, we report for the first time that fluoroether electrolytes can enable reversible lithium intercalation within graphite and suppress undesired solvent co-intercalation. Using XRD, Raman, and NMR spectroscopy, we prove that fluoroether electrolytes enable the conventional lithium intercalation mechanism to form Li_xC_6 without solvent co-intercalation. In Graphite/$LiFePO_4$ full cells, fluoroether electrolytes mirror the performance of carbonate electrolyte at 20°C and outperform glyme ethers. Fluoroether electrolytes show better thermal stability than carbonate electrolytes by supporting stable cycling at 60°C. Remarkably, we show that fluoroether electrolytes enable novel silicon-based Li-ion full cells as single-solvent-single-salt electrolytes while carbonate electrolytes struggle even with FEC and VC additives. Finally, we show that the reductive degradation of fluoroether solvents contributes to the passivation of graphite, which likely suppresses solvent co-intercalation. Our electrolyte chemistry approach opens a new direction for developing novel carbonate-free electrolytes that expand the deployment of Li-ion batteries in different applications and enable novel battery chemistries for next generation Li-ion batteries.

Experimental section

Materials

E3F1, E4F1 and E5F1 compounds were synthesized according to published procedures.[27] 1 M $LiPF_6$ in EC/DMC (1:1 volume ratio, battery grade), diglyme (anhydrous), dimethoxy ethane (DME, anhydrous), fluoroethylene carbonate (⩾99%, acid <200 ppm, anhydrous) and 4 Å molecular sieves were purchased from Sigma-Aldrich. The 1.2 M LiPF6 in EC/EMC/DEC+2% FEC+1%VC (EC/EMC/DEC+FEC/VC) electrolyte was kindly provided by Nanograf Corporation. Lithium bis(fluorosulfonyl) amide (LiFSA, 99%) was purchased from Oakwood Chemical. Deuterated water (≥99.8 atom % D) and deuterated chloroform (≥99.8 atom % D) were purchased from Cambridge Isotope Laboratories. All solvents used for preparing electrolytes were dried by 4 Å molecular sieves overnight and stored with molecular sieves inside an Argon-filled glovebox (VigorTech, O_2 and H_2O < 1 ppm). LiFSA salt was vacuum dried at 120°C overnight in a heated glovebox antechamber before use and was not exposed to air at any time. Other chemicals were used as received.

Celgard 2325 and 3501 separators were purchased from Celgard LLC. Celgard separators were cut into 18 mm disks. Celgard 2325 separator was rinsed with acetone and vacuum dried at 70°C while Celgard 3501 separator was directly vacuum dried at 70°C. Separator disks were moved into an Argon-filled glovebox (O_2 and H_2O < 1 ppm) without air exposure before use. All coin cell parts were obtained from Xiamen TOB New Energy Technology. Lithium foil (750 µm thick) was purchased from Alfa Aesar. Lithium foils were polished with a brush to remove oxide layer and cut into 12 mm diameter disks before use. Graphite, graphite-silicon (Gr-Si) and $LiFePO_4$ (LFP) electrodes were provided by Cell Analysis, Modeling, and Prototyping (CAMP) facility of Argonne National Laboratory. Graphite electrode has a total mass loading of 6.35 mg/cm^2 with 91.83 wt% of Hitachi MagE3 graphite, 2 wt% of Timcal C45 carbon, 6 wt% of Kureha 9300 PVDF binder and 0.17 wt% of oxalic acid. Gr-Si electrode has a total mass load of 3.63 mg/cm^2 with 73 wt% of Hitachi MagE3 graphite, 15 wt% of Paraclete Energy Silicon and 2 wt% of Timcal C45 carbon, 10 wt% of LiOH titrated LiPAA (H_2O). LFP electrode has a total mass loading of 13.40 mg/cm^2 with 90 wt% of Johnson Matthey LFP, 5 wt% of Timcal C45 carbon and 5 wt% of Solvay 5130 PVDF binder. Graphite, Gr-Si and LFP electrodes were cut into 12 mm diameter disks, dried at 120°C overnight in a heated glovebox antechamber before use. Graphite electrode using styrene-butadiene rubber (SBR) binder was prepared by mixing 90 wt% of graphite particle (Graphite anode material for high power applications, Electrodesandmore) and 10 wt% of SBR (Electrodesandmore) into an aqueous slurry and blade casting the slurry on copper foil. The electrode sheet was first dried in air and cut into 12 mm diameter disks. Electrode disks were then dried at 120°C overnight in a heated glovebox antechamber before use.

Electrochemical characterizations

Coin cell preparation: All the electrochemical characterizations except for *in situ* XRD test were performed in CR2032 type coin cells with the following configuration: negative case||spring||spacer||anode (counter electrode)||30 μL electrolyte||1 separator||30 μL electrolyte||cathode (working electrode)||spacer||positive case. Celgard 2325 separator was used for most of the electrolytes except for 1 M $LiPF_6$ in EC/DMC, where Celgard 3501 was used for better wetting. All the coin cells were assembled inside an Argon-filled glovebox (O_2 and H_2O < 1 ppm).

Cyclic voltammetry (CV): CV was performed in coin cells using graphite as working electrode and lithium metal as counter and reference electrode (termed Li/Gr cells). A Biologic MPG-2 Potentiostat was used to test Li/Gr cells at 20°C. After resting for 3 hours, cell voltage was scanned from open circuit voltage to 0.01 V and then reverse scanned to 2.5 V at a scan rate of 0.05 mV s^{-1}.

Coin cell cycling: A Neware BTS4000 battery tester was used to cycle Li/Gr, Li/Gr-Si, Gr/LFP and Gr-Si/LFP coin cells. All cells were rested for 10 hours before testing. For the cycling test at elevated temperature, a Memmert IN 110 oven was used to hold the temperature at 60°C. dQ/dV analysis of graphite intercalation voltage profiles in Li/Gr cells was performed using a python script, in which dQ/dV values were calculated for 1~3 mV intervals.

Electrochemical impedance spectroscopy (EIS): Gr/LFP coin cells were first cycled three times at a current rate of C/20 (ending with deintercalation). Afterward, a Biologic VSP-300 Potentiostat was used to measure impedance spectra between 7 MHz and 1 Hz at 20°C. Fitting of EIS curves was performed using EC-lab software package (V11.33).

Physical characterization

***ex situ* X-ray diffraction (XRD):** Intercalated Gr or Gr-Si electrodes were retrieved from Li/Gr or Li/Gr-Si coin cells after intercalating for 20 hours or to 0.01 V at a current rate of C/20. Coin cells were disassembled inside an argon glovebox. Electrolyte residue was carefully wiped off the surface of intercalated graphite and the electrodes were dried under vacuum. Diglyme sample was tested directly without vacuum drying to preserve the structure of solvent co-intercalated GIC. Deintercalated graphite electrodes were retrieved from Gr/LFP cells after three formation cycles at C/20 (ending with deintercalation). Gr/LFP cells were dissembled in an argon glovebox. Graphite electrodes cycled in ether electrolytes were washed with anhydrous DME while EC/DMC sample was washed with anhydrous DMC three times and dried under vacuum to remove electrolyte residue. Kapton board and tapes were used to seal as prepared graphite electrode before moving out of glovebox and testing at a Rigaku SmartLab X-ray diffractometer. The instrument is equipped with a HyPix3000 detector. All measurements were carried out with a Cu Ka radiation (1.54186 Å). Scans were measured using a parallel beam mode selected through the attached Cross Beam Optics. The tube was energized at 44 mA and 40 kV. The data collections were completed in SmartLab Studio II software package (version 4.4.241.0).

Raman spectroscopy: Intercalated and deintercalated graphite electrodes were prepared following the procedure described in XRD section. For Raman spectroscopy, graphite sample was sealed in glass chambers inside an argon filled glovebox. The glass chamber was assembled using glass slides (Chemglass life science) and silicone isolators purchased from Grace Bio-Labs. Raman spectra were collected using a HORIBA LabRAM HR Evolution Confocal Raman Microscope equipped with a 633 nm laser as light source. The laser power was carefully controlled to ensure stable spectra during the data collection process.

***in situ* synchrotron XRD:** Li/Gr cells with Kapton window were prepared in the configuration described in Fig. S4. The *in situ* experiments were performed at 13 BMC beamline of Advanced Photon Source at Argonne National Laboratory. The beamline has an energy of 28.6 keV, corresponding to $\lambda = 0.43409$ Å. θ angles were converted to Cu Ka scale when plotting the data to avoid confusion.

Solid state MAS NMR: ^{7}Li, ^{1}H and ^{19}F MAS NMR experiments were performed using a Bruker Avance III wide bore 400 MHz solid state NMR spectrometer (9.5 Tesla). Intercalated graphite electrodes were retrieved from Li/Gr cells as described above except that diglyme sample was vacuum dried to ensure complete removal of solvent residue. In an argon glovebox, intercalated graphite powder was scraped off Cu substrate using a plastic scraper and packed in 1.9 mm zirconia rotors. Rotors were spun at 20 kHz and spectra were acquired with a recycle delay time of 30-50 seconds depending on the sample. Spectra intensities were normalized to the mass of the sample (9-11 mg) and scaled according to the number of scans taken for each sample.

Transmission electron microscopy (TEM): Graphite electrode cycled in E3F1 electrolyte for 3 formation cycles (end on deintercalation) was retrieved following the procedure described in XRD section. Lamella of graphite sample was prepared by “lift-out” method using a FEI Helios Nanolab SEM/FIB. TEM imaging and EDS mapping was performed with a JEOL ARM200CF Aberration-Corrected TEM.

X-ray photoelectron spectroscopy (XPS): Graphite electrode using styrene-butadiene rubber (SBR) as binder was used to assemble Li/Gr cells with different electrolytes. Li/Gr cells were cycled at C/20 three times (ending with deintercalation). Coin cells were disassembled inside an argon filled glovebox. Graphite electrode was retrieved, rinsed with anhydrous DME for three times to remove electrolyte residue and dried under vacuum. XPS analysis was performed by the PHI 5000 VersaProbe II System (Physical Electronics). The spectra were obtained using an Al Ka radiation (hν = 1486.6 eV) beam (100 μm, 25 W), Ar^+ and electron beam sample neutralization, in Fixed Analyzer Transmission mode. XPS spectra were aligned to the C−C component in the C1s spectra at 284.6 eV. Peak fitting was completed in Origin 8.5 software with gaussian curves.

NMR spectroscopy for SEI extraction: Cycled graphite electrodes were retrieved from Gr/LFP cells following the procedure described in XRD section. Two pieces of cycled graphite electrodes were rinsed by 0.5 mL of D_2O for 30 mins. Liquid phase was filtered and filled in an NMR tube. The NMR tube was capped and sealed by PTFE film and parafilm inside glovebox to avoid any air exposure. ^{1}H and ^{19}F NMR spectra were collected with a Bruker Ascend 9.4 T / 400 MHz instrument.

Simulations

Density functional theory (DFT) calculations: DFT calculations were performed using the Gaussian 16 computational package.[44] All geometries were optimized at B3LYP/6-31G(d,p) level of theory. After stationary points were verified by the absence of imaginary frequency, single point energies of the optimized geometries were calculated using B3LYP/6-311++G(d,p). Solvent effects were accounted by employing SMD model.[45] THF was selected for ether solvents because of its moderate dielectric constant while methanol was selected for EC according to the reported dielectric constant of EC/DMC mixture.[46] Grimme's DFT-D3 method with BJ-damping (GD3BJ) was used for dispersion correction.[47] Adiabatic reduction potential is defined as the electrochemical potential of single electron reduction ($M + e^- \rightarrow M^-$), where the geometry of product (M^-) is optimized. The reduction energy was calculated from $G(M) - G(M^-)$. The energy value was divided by Faraday's constant and then 1.4 V was subtracted from it to convert to reduction potentials versus Li/Li$^+$ electrode.[48]

Supporting Information

Additional data and Figures. Battery cycling data, optical images, Raman spectra, XRD data, NMR data, TEM images, EDS data, XPS spectra and EIS data.

Author Contributions

C.V.A. and Peiyuan Ma conceived the idea and designed the experiments. Peiyuan Ma performed the synthesis, electrochemical characterizations, cycling tests, Raman spectroscopy, solution state NMR and DFT calculations. Priyadarshini Mirmira performed the solid state NMR. P.J.E. conducted the *in situ* XRD experiments. S.S. and I.D.B. collected the XPS spectra. A.S.F. helped with *ex situ* XRD experiments. All author contributed to the discussion. Peiyuan Ma and C.V.A. wrote the manuscript, and all the authors contributed to editing the manuscript.

Conflicts of interest

There are no conflicts of interest to declare.

Acknowledgments

This work was supported by generous start-up funds from the University of Chicago, the Neubauer Family Assistant Professors program, Sloan Scholar Mentoring Network seed grant, and the 3M Nontenured Faculty Award. This work made use of the shared facilities (Raman) at the University of Chicago Materials Research Science and Engineering Center, supported by the National Science Foundation under award number DMR-2011854. Solution-state NMR measurements were performed at the UChicago Chemistry NMR Facility, and solid-state NMR experiments were performed at the University of Illinois at Chicago NMR facility (NIH award 1S10RR025105-01). DFT calculations were performed with resources provided by the University of Chicago's Research Computing Center. This research used resources of the Advanced Photon Source, a U.S. Department of Energy (DOE) Office of Science user facility operated for the DOE Office of Science by Argonne National Laboratory under Contract No. DE-AC02-06CH11357. We acknowledge the support of GeoSoilEnviroCARS (Sector 13), which is supported by the National Science Foundation - Earth Sciences (EAR-1634415). The authors thank Paul Smeets and Xiaobing Hu at Northwestern University's NUANCE facility for help with TEM, Timothy T. Fister and Di Wang for fruitful discussions on XRD, and Steve Trask and Andrew Jansen at Argonne's Cell Analysis, Modeling, and Prototyping (CAMP) facility for providing the graphite, graphite-silicon and LFP electrodes. I.D.B. and S.S. gratefully acknowledge support from Samuel Gillard at the U. S. Department of Energy (DOE), Vehicle Technologies Office. Argonne National Laboratory is operated for the DOE Office of Science by UChicago Argonne, LLC, under contract number DE-AC02-06CH11357.

References

1. Winter, M., Barnett, B. & Xu, K. Before Li Ion Batteries. *Chem. Rev.* **118**, 11433–11456 (2018).
2. Zuo, X., Zhu, J., Müller-Buschbaum, P. & Cheng, Y.-J. Silicon based lithium-ion battery anodes: A chronicle perspective review. *Nano Energy* **31**, 113–143 (2017).
3. Ohzuku, T., Ueda, A. & Yamamoto, N. Zero-Strain Insertion Material of Li [Li1 / 3Ti5 / 3] O 4 for Rechargeable Lithium Cells. *J. Electrochem. Soc.* **142**, 1431–1435 (1995).
4. Lee, W. *et al.* Advances in the Cathode Materials for Lithium Rechargeable Batteries. *Angew. Chemie Int. Ed.* **59**, 2578–2605 (2020).
5. Xu, K. Nonaqueous Liquid Electrolytes for Lithium-Based Rechargeable Batteries. *Chem. Rev.* **104**, 4303–4418 (2004).
6. Michan, A. L. *et al.* Solid Electrolyte Interphase Growth and Capacity Loss in Silicon Electrodes. *J. Am. Chem. Soc.* **138**, 7918–7931 (2016).
7. Wu, H. & Cui, Y. Designing nanostructured Si anodes for high energy lithium ion batteries. *Nano Today* **7**, 414–429 (2012).
8. Jung, R. *et al.* Consumption of Fluoroethylene Carbonate (FEC) on Si-C Composite Electrodes for Li-Ion Batteries. *J. Electrochem. Soc.* **163**, A1705–A1716 (2016).
9. Xu, K. Electrolytes and Interphases in Li-Ion Batteries and Beyond. *Chem. Rev.* **114**, 11503–11618 (2014).
10. Amanchukwu, C. V, Harding, J. R., Shao-Horn, Y. & Hammond, P. T. Understanding the Chemical Stability of Polymers for Lithium–Air Batteries. *Chem. Mater.* **27**, 550–561 (2015).
11. McCloskey, B. D., Bethune, D. S., Shelby, R. M., Girishkumar, G. & Luntz, A. C. Solvents' Critical Role in Nonaqueous Lithium–Oxygen Battery Electrochemistry. *J. Phys. Chem. Lett.* **2**, 1161–1166 (2011).
12. Amanchukwu, C. V, Kong, X., Qin, J., Cui, Y. & Bao, Z. Nonpolar Alkanes Modify

Lithium-Ion Solvation for Improved Lithium Deposition and Stripping. *Adv. Energy Mater.* **9**, 1902116 (2019).

13. Chen, J. *et al.* Electrolyte design for LiF-rich solid–electrolyte interfaces to enable high-performance microsized alloy anodes for batteries. *Nat. Energy* **5**, 386–397 (2020).
14. Jache, B., Binder, J. O., Abe, T. & Adelhelm, P. A comparative study on the impact of different glymes and their derivatives as electrolyte solvents for graphite co-intercalation electrodes in lithium-ion and sodium-ion batteries. *Phys. Chem. Chem. Phys.* **18**, 14299–14316 (2016).
15. Kim, H. *et al.* Exploiting Lithium–Ether Co-Intercalation in Graphite for High-Power Lithium-Ion Batteries. *Adv. Energy Mater.* **7**, 1700418 (2017).
16. Moon, H. *et al.* Mechanism of Li Ion Desolvation at the Interface of Graphite Electrode and Glyme–Li Salt Solvate Ionic Liquids. *J. Phys. Chem. C* **118**, 20246–20256 (2014).
17. Yamada, Y. *et al.* Unusual Stability of Acetonitrile-Based Superconcentrated Electrolytes for Fast-Charging Lithium-Ion Batteries. *J. Am. Chem. Soc.* **136**, 5039–5046 (2014).
18. Yamada, Y. *et al.* General Observation of Lithium Intercalation into Graphite in Ethylene-Carbonate-Free Superconcentrated Electrolytes. *ACS Appl. Mater. Interfaces* **6**, 10892–10899 (2014).
19. Yamada, Y., Yaegashi, M., Abe, T. & Yamada, A. A superconcentrated ether electrolyte for fast-charging Li-ion batteries. *Chem. Commun.* **49**, 11194–11196 (2013).
20. Zeng, P. *et al.* A stable graphite electrode in superconcentrated LiTFSI-DME/DOL electrolyte and its application in lithium-sulfur full battery. *Mater. Res. Bull.* **95**, 61–70 (2017).
21. Chen, S. *et al.* High-Voltage Lithium-Metal Batteries Enabled by Localized High-Concentration Electrolytes. *Adv. Mater.* **30**, 1706102 (2018).
22. Jiang, L.-L. *et al.* Inhibiting Solvent Co-Intercalation in a Graphite Anode by a Localized High-Concentration Electrolyte in Fast-Charging Batteries. *Angew. Chemie Int. Ed.* **60**, 3402–3406 (2021).

23. Louli, A. J. *et al.* Diagnosing and correcting anode-free cell failure via electrolyte and morphological analysis. *Nat. Energy* **5**, 693–702 (2020).

24. Amanchukwu, C. V. The Electrolyte Frontier: A Manifesto. *Joule* **4**, 281–285 (2020).

25. Amanchukwu, C. V *et al.* A New Class of Ionically Conducting Fluorinated Ether Electrolytes with High Electrochemical Stability. *J. Am. Chem. Soc.* **142**, 7393–7403 (2020).

26. Yu, Z. *et al.* Molecular design for electrolyte solvents enabling energy-dense and long-cycling lithium metal batteries. *Nat. Energy* **5**, 526–533 (2020).

27. Ma, P., Mirmira, P. & Amanchukwu, C. V. Effect of Building Block Connectivity and Ion Solvation on Electrochemical Stability and Ionic Conductivity in Novel Fluoroether Electrolytes. *ACS Cent. Sci.* **7**, 1232–1244 (2021).

28. Yu, Z. *et al.* Rational solvent molecule tuning for high-performance lithium metal battery electrolytes. *Nat. Energy* **7**, 94–106 (2022).

29. Yang, J. *et al.* Molecular Engineering to Enable High-Voltage Lithium-Ion Battery: From Propylene Carbonate to Trifluoropropylene Carbonate. *ACS Energy Lett.* **6**, 371–378 (2021).

30. Ohzuku, T., Iwakoshi, Y. & Sawai, K. Formation of Lithium-Graphite Intercalation Compounds in Nonaqueous Electrolytes and Their Application as a Negative Electrode for a Lithium Ion (Shuttlecock) Cell. *J. Electrochem. Soc.* **140**, 2490–2498 (1993).

31. Reynier, Y., Yazami, R. & Fultz, B. XRD evidence of macroscopic composition inhomogeneities in the graphite–lithium electrode. *J. Power Sources* **165**, 616–619 (2007).

32. He, H., Huang, C., Luo, C.-W., Liu, J.-J. & Chao, Z.-S. Dynamic study of Li intercalation into graphite by in situ high energy synchrotron XRD. *Electrochim. Acta* **92**, 148–152 (2013).

33. Sole, C., Drewett, N. E. & Hardwick, L. J. In situ Raman study of lithium-ion intercalation into microcrystalline graphite. *Faraday Discuss.* **172**, 223–237 (2014).

34. Letellier, M., Chevallier, F. & Morcrette, M. In situ 7Li nuclear magnetic resonance

observation of the electrochemical intercalation of lithium in graphite; 1st cycle. *Carbon N. Y.* **45**, 1025–1034 (2007).

35. Kim, H. *et al.* Sodium intercalation chemistry in graphite. *Energy Environ. Sci.* **8**, 2963–2969 (2015).
36. Ravdel, B. *et al.* Thermal stability of lithium-ion battery electrolytes. *J. Power Sources* **119–121**, 805–810 (2003).
37. Zhang, X. *et al.* Advanced Electrolytes for Fast-Charging High-Voltage Lithium-Ion Batteries in Wide-Temperature Range. *Adv. Energy Mater.* **10**, 2000368 (2020).
38. Sloop, S. E., Pugh, J. K., Wang, S., Kerr, J. B. & Kinoshita, K. Chemical Reactivity of PF5 and LiPF6 in Ethylene Carbonate/Dimethyl Carbonate Solutions. *Electrochem. Solid-State Lett.* **4**, A42 (2001).
39. Xu, K. Whether EC and PC Differ in Interphasial Chemistry on Graphitic Anode and How. *J. Electrochem. Soc.* **156**, A751 (2009).
40. Nie, M. *et al.* Lithium Ion Battery Graphite Solid Electrolyte Interphase Revealed by Microscopy and Spectroscopy. *J. Phys. Chem. C* **117**, 1257–1267 (2013).
41. Lu, D. *et al.* Formation of Reversible Solid Electrolyte Interface on Graphite Surface from Concentrated Electrolytes. *Nano Lett.* **17**, 1602–1609 (2017).
42. Jia, H. *et al.* Enabling Ether-Based Electrolytes for Long Cycle Life of Lithium-Ion Batteries at High Charge Voltage. *ACS Appl. Mater. Interfaces* **12**, 54893–54903 (2020).
43. Ming, J. *et al.* New Insights on Graphite Anode Stability in Rechargeable Batteries: Li Ion Coordination Structures Prevail over Solid Electrolyte Interphases. *ACS Energy Lett.* **3**, 335–340 (2018).
44. Frisch, M. J. *et al.* Gaussian 16 Rev. A.03. (2016).
45. Marenich, A. V, Cramer, C. J. & Truhlar, D. G. Universal Solvation Model Based on Solute Electron Density and on a Continuum Model of the Solvent Defined by the Bulk Dielectric Constant and Atomic Surface Tensions. *J. Phys. Chem. B* **113**, 6378–6396 (2009).

46. Daniels, I. N., Wang, Z. & Laird, B. B. Dielectric Properties of Organic Solvents in an Electric Field. *J. Phys. Chem. C* **121**, 1025–1031 (2017).

47. Grimme, S., Ehrlich, S. & Goerigk, L. Effect of the damping function in dispersion corrected density functional theory. *J. Comput. Chem.* **32**, 1456–1465 (2011).

48. Borodin, O., Behl, W. & Jow, T. R. Oxidative Stability and Initial Decomposition Reactions of Carbonate, Sulfone, and Alkyl Phosphate-Based Electrolytes. *J. Phys. Chem. C* **117**, 8661–8682 (2013).